中華民國第三十一屆電力工程研討會
台灣　台南　2010 年 12 月 3-4 日

具可升壓直流鏈永磁同步馬達驅動之衛星反應輪
A PMSM Driven Satellite Reaction Wheel with Voltage Boostable DC-link

周明昌　　廖聰明
Ming-Chang Chou　　Chang-Ming Liaw

國立清華大學 電機工程學系
Department of Electrical Engineering, National Tsing Hua University
Hsinchu, Taiwan, R.O.C.
E-mail：cmliaw@ee.nthu.edu.tw

摘 要

本文旨在建構一永磁同步馬達驅動之反應輪系統，其直流鏈電壓可隨反應輪轉速調升以於廣速範圍內具有良好線圈電流追控特性。所有功率級之數位控制採單一共同數位信號處理器實現。於所建構之永磁馬達驅動反應輪系統中，電流迴路含PI迴授控制器隨速度調適之共振控制器及一強健追控誤差消除控制器，以得緊密之弦波線圈電流命令追控。在速度控制方面，採行簡易之強健模式追隨控制。接著構建一直流/直流升壓前級，由變動之太陽電池直流源建立一可升及穩定之直流鏈電壓。藉由規劃隨速度變動之直流鏈電壓，可使反應輪系統在直流電源變動下，於廣速範圍內具良好之驅動性能。此外亦構裝一動態煞車機構，獲得穩定之馬達煞車操作特性。

關鍵字：反應輪、永磁同步馬達、電流控制、速度控制、數位信號處理器、前端轉換器、電壓升壓。

Abstract

This paper presents a permanent magnet synchronous motor (PMSM) driven satellite reaction wheel, its DC-link voltage is boostable in accordance with wheel speed to yield good winding current tracking control under wide speed range. The digital controls of all power stages are realized in a common digital signal processor (DSP). First, the PMSM driven reaction wheel is established. In its current controlled PWM scheme, the PI feedback controller is augmented with a speed adaptive resonant controller and a robust tracking error cancellation controller to yield precise sinusoidal winding current command tracking. That followed a simple robust model following speed control scheme is designed. Then a DC/DC boost front-end converter is developed to establish boostable and well-regulated DC-link voltage from the fluctuated photovoltaic DC source. The speed-dependent DC-link voltage is set to obtain good wheel driving performance under wide speed range and varied DC source voltage. In addition, the chopping dynamic braking mechanism is also equipped to yield stable braking operation.

Keywords: Reaction wheel, PMSM, current control, speed control, DSP, front-end converter, voltage boosting.

I. INTRODUCTION

Motor driven reaction wheel is a key component in making attitude control for a satellite [1-4]. The attitude control is achieved via regulating the inverter-fed motor developed torque. Normally, the main source of this system is provided by photovoltaic (PV) cell, which is fluctuated in power and voltage level. Hence the followed DC/DC converter is generally required to establish regulated DC-link voltage for the followed motor drive. Moreover, the suited energy storage buffer is also required to reserve the power supporting reliability. Recently, some researches are emphasized on the development of integrated energy storage and attitude control with two flywheels [3,4].

Compared with other used motors, PMSM is more suited to be the actuator for reaction wheel owing to its superior features [5,6]. To let a PMSM drive possess good driving performance, current control is the first key issue. However, for a sine-wave PMSM drive, the close varying frequency current tracking control under the existence of back-EMF and the parameter variations is not a trivial issue. The resonant feedback control is the simple and effective means in handling this issue [7-10]. In [10], the improved current control scheme with adaptive resonant feedback control and robust control has been developed to yield better current tracking control for a PMSM driven reaction wheel. However, the regulation of DC-link voltage in accordance with the fluctuated PV voltage and wheel speed is not considered.

It is well known that the speed-dependent back-EMF will degrade the motor winding current dynamic response. Field-weakening and voltage boosting are two commonly adopted methods to reduce the effects of back-EMF. In [11-13], the comparative performance studies have been conducted for the PMSM drives under these two control approaches. The results showed that voltage boosting yields higher efficiency than field-weakening under constant power region. For the PV powered PMSM drive, the equipment of DC/DC boost converter front-end can naturally achieve the voltage boosting control task.

Some researches concerning the development and applications of boost DC/DC converters for motor drives have been presented in [12-19]. In [12], the efficiency and cost-effectiveness of direct battery and DC/DC boosted AC drives for EV applications have been investigated in the aspects of sizing and power losses. The comparative results show that the cost and losses are considerably reduced by the boost-based system. In [13], a charge-pumped boost drive using electric double-layer capacitors is proposed to reduce the input power peaks. As to the research made in [15], the battery voltage is boosted to power the motor drive in the commercial HEV THS-II to avoid the additional copper loss caused by field-weakening. In addition, the bidirectional buck-boost converters used for EV motor drive are developed in [16,17]. Two commonly adopted topologies are studied in [17], and the cascade one possesses the less inductor average and ripple current. The front-end DC/DC buck-boost converters are also employed for PMSM drives in [18,19] to let the DC-link voltage be lower than the battery voltage in low speeds.

In real operation, the boosted DC-link voltage should be properly set to achieve better driving performance and efficiency. In [14], the DC-link voltage command is set according to the d- and q-axis voltages being yielded from regulating the current tracking errors. In [15], four types of losses are taken into consideration in deciding the variable DC-link voltage. Basically, the system voltage is set approximately equal to the motor back-EMF. In low speed, the lowest voltage of the boost converter, i.e., the battery voltage, is set. And the maximum system voltage is set under high speed. Within intermediate speed range, the system voltage is varied according to the speed to minimize

the total losses. As to [18,19], the equipment of buck-boost converter allows the DC-link voltage to be set lower than the battery voltage, hence the reduction of losses under constant torque operation is achieved.

In this paper, a DSP-based PMSM driven satellite reaction wheel with DC-link voltage boosting is first established. In its current control scheme, a PI feedback controller is augmented with a speed adaptive resonant controller and a robust tracking error cancellation controller, the precise sinusoidal winding current command tracking control is obtained in wide speed range under reasonable DC-link voltage levels. Then the robust speed control is conducted to yield the desired speed dynamic response. Finally, a DC/DC boost front-end converter is developed to establish boostable and well regulated DC-link voltage from the fluctuated PV DC source. The boost converter output voltage is set according to the motor speed to obtain good wheel driving performance under varied speed and DC source voltage. All control algorithms are realized in a common DSP. Some measured results are provided to verify driving performance of the established reaction wheel.

II. System Configuration and Problem Statement

A. System Configuration

The developed PMSM driven reaction wheel is shown in Figs. 1(a) to 1(d), the constituted components are introduced as followed:

- PV DC source: $V_{dc} = 22 \sim 38\text{V}$, a DC power supply is used as a test source here.
- Boost converter front-end: it is used to provide a stable DC-link voltage for the followed inverter from the varied PV DC source.
- Dynamic brake: a chopping controlled resistor is placed in DC-link to dynamically absorb the regenerating energy during deceleration period and stably regulate the DC-link voltage. Besides, the dynamic brake can also be used as a dummy load of the boost front-end converter to stabilize the DC-link voltage at light load.
- Inverter: it is constructed using the commercialized three-phase intelligent insulated gate bipolar transistor (IGBT) power module IRAMS10UP60 (600V/10Arms) (International Rectifier Corp.).
- PMSM (RBE 01511-C by Kollmorgen Corp.): three-phase Y-connected, 12poles, 131W, 5400rpm.
- Reaction wheel: J= $0.0217\,\text{kg}\cdot\text{m}^2$ (or $\text{N}\cdot\text{m}\cdot\text{s}^2/\text{rad}$), speed $\le 2000\text{rpm}$ ($0 \le f_1 \le 200\text{Hz}$), torque $\le \pm 0.2\text{N}\cdot\text{m}$.
- Digital control board: established using the DSP TMS320F2812 (Texas Instruments).
- Position sensing scheme: 3-phase Hall sensors and an incremental optical encoder with quadrant two phase outputs having 1024 pulses/revolution.
- Control schemes: detailed controller structures of all constituted power stages are shown in Figs. 1(a) to 1(d), their designs will be described in latter paragraphs.

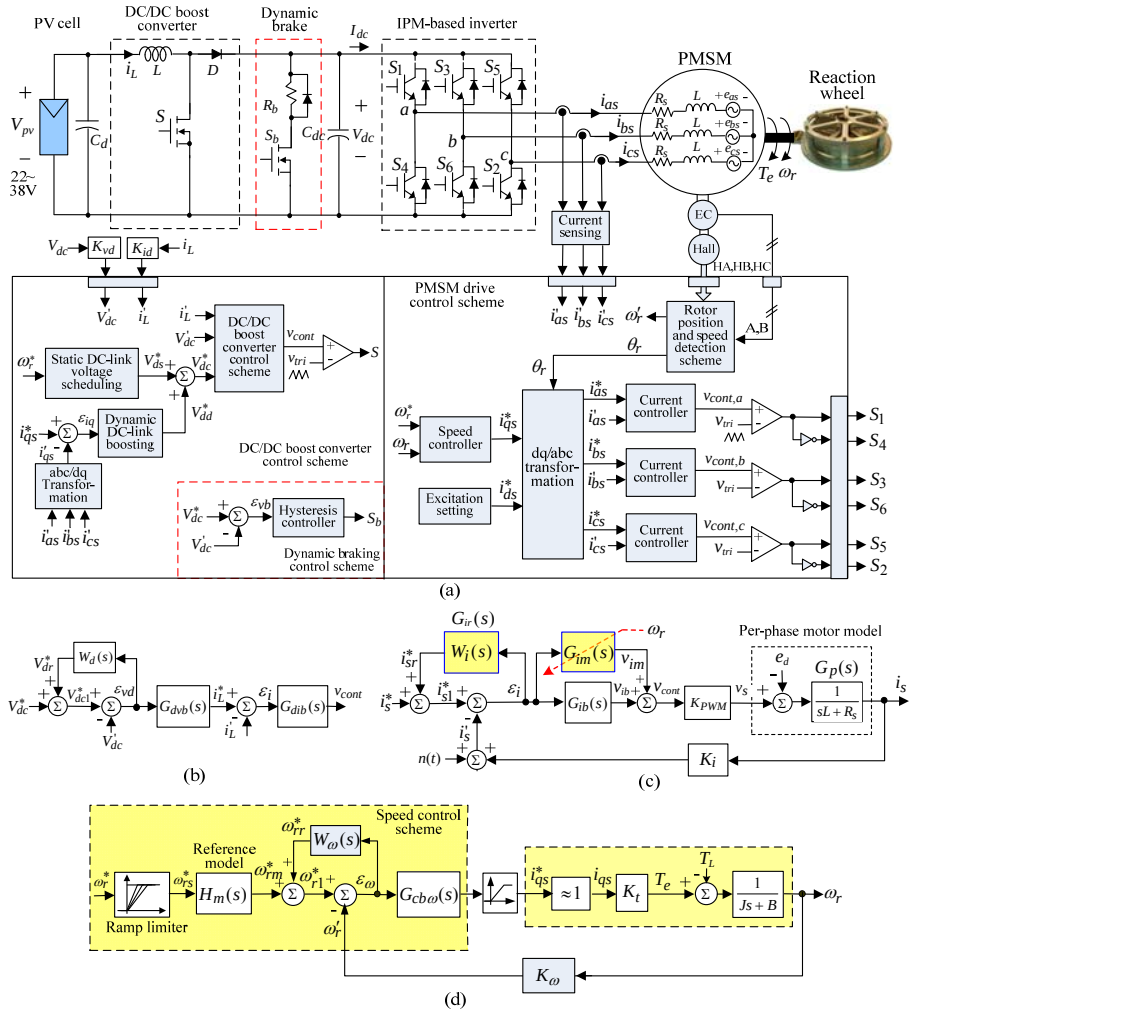

Fig. 1. The developed PMSM driven reaction wheel: (a) system configuration; (b) DC/DC boost converter control scheme; (c) per-phase winding current control scheme; (d) speed control scheme.

B. Problem Statement

(a) Normal DC-link voltage

If the DC-link voltage established from PV-source is sufficiently high for the rotor speed and load, the PMSM winding tracking control can be achieved successfully applying proper dynamic control approach. The current control of a PMSM drive can be conducted in either dq- or abc-domain. Because of the merits of using less frame transformation and the more direct control in manipulating physical motor winding current, the current control in abc-domain is adopted in this paper. The proposed current control scheme is shown in Fig. 1(c), wherein the PI feedback controller is augmented by a adaptive resonant controller and a robust error cancellation controller (RECC) [10]. As to the proposed speed control scheme shown in Fig. 1(d), a simple robust reference model following controller and a speed command ramp limiter are arranged to yield proper speed response profile without causing winding current saturation.

(b) DC-link voltage boosting

Through proper derivation [5,10], the phase winding voltage equation (phase-a as an example of a PMSM) can be expressed as:

$$v_{as} = R_s i_{as} + [L_{ls} + \frac{3}{2}(L_A + L_B)]\frac{d}{dt} i_{as} + e_{as} \triangleq R_s i_{as} + L_q \frac{d}{dt} i_{as} + e_{as} \quad (1)$$

$$e_{as} = \omega_r \lambda'^r_m \cos\theta_r \triangleq \hat{E}_{as} \cos\theta_r, \quad \theta_r = \theta_r(0) + \int_0^t \omega_r(\xi) d\xi \quad (2)$$

where R_s = winding resistance, λ'^r_m = amplitude of flux linkage established by rotor permanent magnets, and the nominal winding inductance is chosen as $\bar{L} = L_q$ which is the q-axis inductance. The measured key parameters of the employed PMSM are:

- $\lambda'^r_m = 0.00858$ Web .
- $\hat{E}_d = 5.39$V(1000rpm), 10.78V(2000rpm) .
- Equivalent torque constant $K_t = 3P/4\,\lambda'^r_m = 0.07722\,\text{N}\cdot\text{m/A}$.
- $L_q = 328.415\mu$H , $L_d = 214.635\mu$H (at $f = 200$Hz).
- Average per-phase winding resistance $\bar{R}_s = 0.60625\Omega$.

From (1) the winding current changing rate can be expressed as:

$$\frac{d}{dt} i_{as} = \frac{v_{as} - R_s i_{as} - e_{as}}{L_q} \quad (3)$$

It is obviously from (2) and (3) that the increasing speed-dependent back-EMF e_{as} will limit the current dynamic response. Some possible remedies lie in: (i) field-weakening: this task can be achieved through proper excitation control or commutation advanced shift. However, the motor efficiency will be lowered, and the risk of permanent magnet demagnetization should be cared; (ii) applying modified PWM technique to slightly increase the voltage utilization, but the boosting capability is limited; and (iii) voltage-boosting: it is the most effective means. In the developed system shown in Fig. 1(a), a DC/DC boost front-end is equipped to provide boostable DC-link voltage for the PMSM drive from the fluctuated PV cell.

III. CONTROL SCHEMES OF PMSM DRIVE

A. Winding Current Control Scheme

Fig. 1(c) shows the per-phase current control block with its model being deduced from (1) with $L \triangleq L_q$ and $e_d \triangleq e_{as}$. The proposed current control scheme consists of a resonant feedback controller $G_{im}(s)$, a PI feedback controller $G_{ib}(s)$ and a robust tracking error cancellation controller (RECC) $G_{ir}(s)$ with a weighting function $W_i(s)$, the transfer functions of these controllers are listed below:

$$G_{im}(s) = \frac{K_{Mi} s}{s^2 + \omega_r^2}, \quad G_{ib}(s) = \frac{K_{Pi} s + K_{Ii}}{s} \quad (4)$$

$$W_i(s) = \frac{W_i}{\tau_i s + 1}, \; 0 \le \text{W}_\text{i} < 1 \quad (5)$$

where W_i denotes a weighting factor, and the low-pass cut-off frequency of $W_i(s)$ is $f_{ci} = 1/(2\pi\tau_i)$. Good and robust sinewave current command tracking and back-EMF rejection controls can be achieved. The compromise of robust control is made by properly choosing the values of W_i and f_{ci} .

(i) Performance Analysis

All closed-loop transfer functions of the whole control scheme shown in Fig. 1(c) as:

$$H_{dr}(s) = \left.\frac{i'_s}{i^*_s}\right|_{e_d=0}, \quad H_{de}(s) = \left.\frac{\varepsilon_i}{i^*_s}\right|_{e_d=0}, \quad H_{dd}(s) = \left.\frac{i'_s}{e_d}\right|_{i^*_s=0} \quad (6)$$

Carful analysis can deduce the following facts [10]:

(a) $G_{im}(s)$ Only:

- $|H_{dr}(j\omega_r)| = 1$ and $|H_{de}(j\omega_r)| = 0$, i.e., the perfect current tracking responses can only be achieved critically at the fundamental frequency.
- $|H_{dd}(s = j\omega_r)| = 0$, the perfect back-EMF rejection is also obtained only at fundamental frequency by $G_{im}(s)$.

(b) $G_{im}(s) + G_{ib}(s)$

- By adding $G_{ib}(s)$ to $G_{im}(s)$, one can find that: (i) $|H_{de}(j\omega_r)| = 0$; (ii) $|H_{de}(0)| = 0$; and (iii) $|H_{de}(j\omega)|$ at other frequencies are much smaller. Hence the closer command waveform tracking control is obtained.
- In addition to the perfect fundamental back-EMF rejection ($|H_{dd}(s = j\omega_r)| = 0$), the better rejection characteristics at other frequencies including DC ($|H_{dd}(0)| = 0$) are also yielded by adding $G_{ib}(s)$ to $G_{im}(s)$.

(c) $G_{im}(s) + G_{ib}(s) + G_{ir}(s)$

- In addition to properties processed by $G_{im}(s) + G_{ib}(s)$, the bandwidth of $H_{dr}(s)$ will be widened by adding $G_{ir}(s)$. Thus the improved current tracking responses for DC and sine-wave with $\omega = \omega_r$ are obtained.
- Similarly, better disturbance rejection will also be obtained over wider frequency range around $\omega = \omega_r$.

(ii) Numerical Design

(a) $G_{im}(s)$

Since the gain K_{Mi} affects only the dynamic behavior around $\omega = \omega_r$, taking the compromised considerations in control performance and control effort, K_{Mi} =100 is chosen to yield:

$$G_{im}(s) = \frac{100s}{s^2 + \omega_r^2} \quad (7)$$

(b) $G_{ib}(s)$

The upper limit of P-gain in $G_{ib}(s)$ is first determined based on the large-signal stability algorithm for a ramp-comparison current controlled PWM (RC-CCPWM) scheme using the known system parameters at maximum operation speed (2000rpm):

$$K_{Pi} \le 0.5446 \quad (8)$$

Accordingly, $K_{Pi} = 0.39$ is chosen. The I-gain of $G_{ib}(s)$ is chosen to be $K_{Ii} = 28.61$ through simulation with resulted loop-gain crossover frequency being f_{cs} = 2.8kHz, which satisfies $f_1 < f_{cs} < 0.5 f_{tri}$ (f_1 =200Hz, f_{tri} =15kHz). Hence,

$$G_{ib}(s)=0.39+\frac{28.61}{s} \tag{9}$$

(c) RECC $G_{ir}(s)$

The current-loop frequency responses of loop gain, $H_{dr}(s)$, $H_{de}(s)$ and $H_{dd}(s)$ under varied motor parameters ($R_s=1.5\bar{R}_s$, $L=0.5\bar{L}$) with different weighting functions are simulated (not shown here). According to the results and taking the compromise considerations between control performance, control effort and noise effects, the following robust control weighting function is chosen:

$$W_i(s)=\frac{0.763}{159.2\times10^{-6}s+1},\ f_{ci}=1\text{kHz} \tag{10}$$

(iii) Experimental Verification

The measured (i_{as}^*, i_{as}') at the nominal case ($V_{dc}=30\text{V}$, $\omega_r^*=1500\text{rpm}$) due to a step speed command change $\omega_r^*=1500\rightarrow1650\text{rpm}$ by three control structures are compared in Fig. 2(a). And the results at another condition ($V_{dc}=34\text{V}$, $\omega_r^*=2000\text{rpm}$, $\omega_r^*=2000\text{rpm}\rightarrow$ 2200rpm) are plotted in Fig. 2(b). During experiment, the speed control scheme, which will be introduced later, is normally actuated. The results indicate that the closer transient and static current waveform tracking response are obtained by the developed controller.

B. Speed Control Loop

(i) Mechanical Model Parameters

For making the speed control loop, the excellent phase current tracking control is assumed that is $i_{qs}'=i_{qs}^*$ and $i_{ds}'=i_{ds}^*$. And the mechanical parameters are also assumed to be constant as the nominal values $K_t=\bar{K}_t=0.07722\,\text{N}\cdot\text{m/A}$, $J=\bar{J}=0.022516\,\text{N}\cdot\text{m}\cdot\text{s}^2/\text{rad}$ and $B=\bar{B}=1.9701\times10^{-4}\ \text{N}\cdot\text{m}\cdot\text{s/rad}$.

(ii) Controller Design

The speed control scheme consists of a PI feedback controller and a simple robust speed tracking error cancellation controller. The latter is added to enhance the speed control dynamics and hence to improve the damping coefficient estimation performance.

(a) PI feedback controller

The PI feedback controller is expressed as:

$$G_{cb\omega}(s)=K_{P\omega}+\frac{K_{I\omega}}{s} \tag{11}$$

With nominal plant model parameters and letting $W_\omega(s)=0$, one can derive the closed-loop speed command tracking transfer function from Fig. 1(d) and Eq. (10) as:

$$H_{d\omega}(s)\overset{\Delta}{=}\left.\frac{\omega_r'(s)}{\omega_{rm}^*(s)}\right|_{T_L(s)=0}=\frac{K_{P\omega}K_\omega\bar{K}_ts+K_{I\omega}K_\omega\bar{K}_t}{\bar{J}s^2+(\bar{B}+K_{P\omega}K_\omega\bar{K}_t)s+K_{I\omega}K_\omega\bar{K}_t} \tag{12}$$

For simplicity, the desired tracking response is specified by a first-order process:

$$H_m(s)=\frac{r}{s+r} \tag{13}$$

Let $H_{d\omega}(s)=H_m(s)$, through careful derivation one can find the controller parameters from (12) and (13) to be:

$$K_{P\omega}=\bar{J}\frac{r}{K_\omega\bar{K}_t},\quad K_{I\omega}=\bar{B}\frac{r}{K_\omega\bar{K}_t} \tag{14}$$

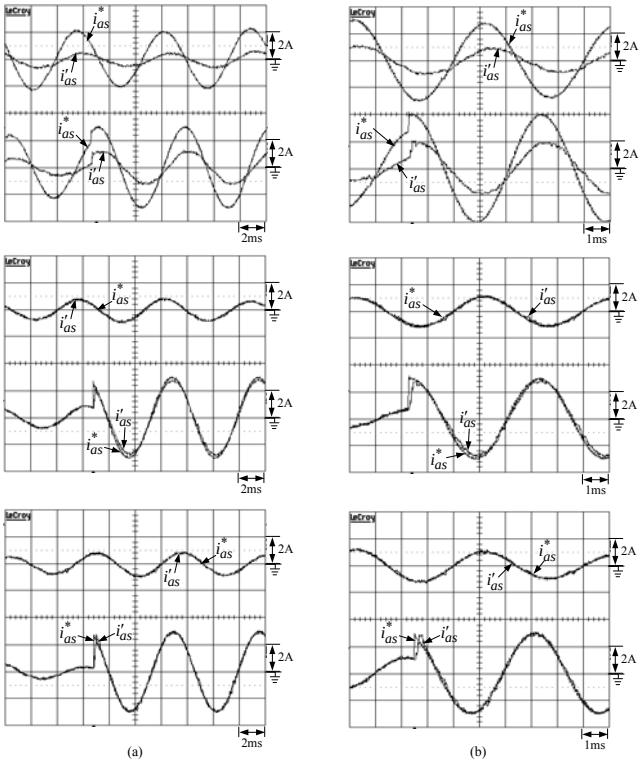

Fig. 2. Measured (i_{as}^*, i_{as}') by $G_{ib}(s)$ only (upper), $G_{ib}(s)+G_{im}(s)$ (middle) and $G_{ib}(s)+G_{im}(s)+G_{ir}(s)$ (lower) at: (a) ($V_{dc}=30V$, 1500rpm) due to a step speed command change $\omega_r^*=1500\rightarrow1650\text{rpm}$; (b) ($V_{dc}=34V$, 2000rpm) due to a step speed command change $\omega_r^*=2000\ \rightarrow2200\text{rpm}$.

According to the response speed achievable by the reaction wheel and the resulted torque current, the reference model $H_m(s)=0.67/(s+0.67)$ (time constant=1.5s) is chosen. Then the controller parameters are found from (14) to yield:

$$G_{cb\omega}(s)=0.020356+\frac{0.000178}{s} \tag{15}$$

(b) Robust speed tracking error cancellation controller

To enhance the robustness of PI feedback control, the tracking error $\varepsilon_\omega=\omega_{rl}^*-\omega_r'$ is regarded as a disturbance, and a robust compensating command $\omega_{rr}^*=W_\omega(s)\varepsilon_\omega$ is generated to reduce the tracking error ($\omega_{rm}^*-\omega_r'$) as far as possible, where $W_\omega(s)$ denotes a weighting function

$$W_\omega(s)=\frac{W_\omega}{1+\tau_\omega s},\quad \tau_\omega=\frac{1}{2\pi f_{c\omega}},\quad 0\le W_\omega<1 \tag{16}$$

Similarly, the weighting factor W_ω is used to determine the extent of robust error cancellation, and the low-pass process $1/(1+\tau_\omega s)$ is arranged to reduce the effects of high-frequency contaminated noise on the closed-loop control behavior. Since the speed fundamental frequency is low, $f_{c\omega}=10\text{Hz}$ is adopted and the weighting factor $W_\omega=0.75$ is chosen. By augmenting the PI feedback controller with the simple robust control, the controlled rotor speed can be made closely follow the defined reference trajectory, i.e., $\omega_r'\approx\omega_{rm}^*$.

For larger magnitude of speed command change, the step command is replaced by ramp command with suitable ramping rate R to avoid long duration of control effort (q-axis current command) saturation.

(iii) Experimental Verification

The designed feedback controller $G_{cb\omega}(s)$ is first tested its performance of reference model tracking. Fig. 3 plots the measured ω_{rm}^*, ω_r', i_{qs}^* and i_{qs}' by the designed feedback controller due to step speed command changes of

$\omega_r = 1000 \rightarrow 1100$rpm at $V_{dc} = 30$V. The result indicates that the reaction wheel speed tracking response meet the reference trajectory defined by $H_m(s) = 0.67/(s+0.67)$.

For larger speed command change, the ramp type command is applied. Fig. 4 shows the measured (ω_{rs}^*, ω_r') and i_{qs}^* due to a ramp speed command change (0 to 2000rpm with $R = 70$rpm/s and $V_{dc} = 30$V) by PI only and the proposed robust controller. The results indicate that better speed tracking response is obtained by applying the proposed robust control, and the torque current commands do not excess the maximum limit value $i_{qsm}^* = 3A$ by properly setting the speed command ramping rate.

IV. DC/DC BOOST CONVERTER AND DYNAMIC BRAKING SCHEME

(i) Specifications and Circuit Components

The developed DC/DC boost converter is operated under continuous conduction mode (CCM) with its specifications being given as: V_{pv} = 22~38V, out power P_o =150W, V_{dc} =30~60V, switching frequency f_{sd} = 50kHz. Accordingly, the circuit component are found as:

- $i_{Sm} = 8.18$A and $v_{Sm} = 60$V, hence the power MOSFET IRFP250 (STMicroelectronics Corp., 200V, 33A) is adopted for both S and S_b.
- $i_{Dm} = 8.18$A and $v_{Dm} = 60$V, thus the power diode DSEP 29-03A (IXYS Corp., 300V, 30A) is adopted .
- For a given inductor ripple current Δi_L, the inductance can be found as:

$$L = \frac{V_{pv} D}{\Delta i_L f_{sd}} \tag{17}$$

where D = duty ratio $= (V_{dc} - V_{pv})/V_{dc}$. By setting $\Delta i_L \triangleq 0.4 i_{L\max}$, the inductance is determined to be $L = 177.97\mu$H as operating at the worse case (V_{pv} =38V, V_{dc} =60V). The inductor is wound using a toroidal core T175-26 (Micrometals Corp.) with 42 turns of AWG#16*2. The measured inductance of the wound inductor is $L = 178.53\mu$H (@50kHz) using LCR meter, Hioki 3532-50.

- The output voltage ripple is

$$\Delta V_{dc} = \frac{D}{C_{dc} f_{sd}} \frac{V_{dc}}{R} \tag{18}$$

with $R = V_{dc}^2 / P_o$ being the equivalent load resistance. By choosing $C_{dc} = 1980\mu F$, the voltage ripple is found as 0.0455% at (V_{pv} =22V, V_{dc} =30V).

- The dynamic braking resistor is chosen to be $R_b = 50\Omega$ (200W).

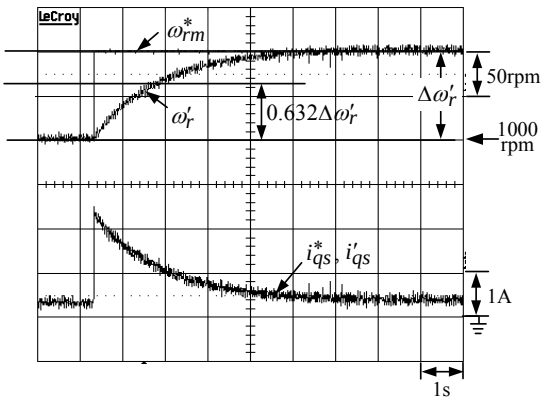

Fig. 3. Measured ω_{rm}^*, ω_r', i_{qs}^* and i_{qs}' at $V_{dc} = 30$V due to a step speed command change from $\omega_r = 1000 \rightarrow 1100$rpm the designed.

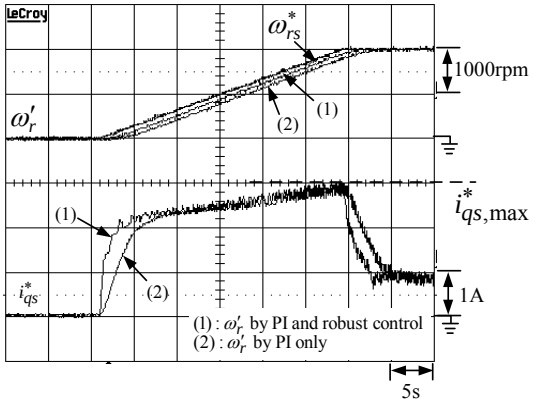

Fig. 4. Measured (ω_{rs}^*, ω_r') and i_{qs}^* due to ramp speed command changes from 0 to 2000rpm by PI controller and the proposed robust controller with ($V_{dc} = 30$V, $R = 70$rpm/s)

(ii) Control Scheme

The proposed control scheme shown in Fig. 1(b) consists of inner ramp-comparison current-controlled PWM (RC-CCPWM) scheme and outer voltage loop.

(a) RC-CCPWM scheme

For simplicity, a PI feedback controller $G_{dib}(s)$ is adopted. In determining its parameters, the large-signal stability criterion is first applied to find the upper limit of P-gain. The ramping rate of control signal should be smaller than that of the saw-tooth carrier:

$$K_{dpi} \frac{d(i_L^* - i_L')}{dt} \le \frac{dv_{tri}}{dt} \tag{19}$$

where i_L^* and $i_L' = K_{id} i_L$ ($K_{id} = 1$V/A is set here) denote the command and sensed variable of inductor current, K_{dpi} is the P-gain of $G_{dib}(s)$. Within a switching period, the inductor current command can be assumed to be constant, hence upper limit of K_{dpi} is found as:

$$K_{dpi} \le \frac{L}{K_{id}(V_{dc} - V_{pv})} 2\hat{v}_{tri} f_{sd} = 0.47 \tag{20}$$

where switching frequency $f_{sd} = 50$kHz, $L = 178.53\mu$H, the amplitude of saw-tooth carrier $\hat{v}_{tri} = 1$V, and $(V_{dc} - V_{pv})$ = (60-22) =38V is set for the worst case.

According to (20), the final values of $G_{dib}(s)$ are determined trail-and-error to be: $G_{dib}(s) = 0.04 + 38.15/s$.

(b) Voltage control scheme

The PI feedback controller $G_{dvb}(s)$ is augmented with a robust tracking error cancellation controller with a weighting function $W_d(s) = W_d/(\tau_d s + 1)$. The parameters of voltage control scheme are chosen by trial-and-error as:

$$G_{dvb}(s) = 0.24 + \frac{1.85}{s} \tag{21}$$

$$W_d(s) = \frac{0.25}{1.59 \times 10^{-3} s + 1} \tag{22}$$

(iii) Experimental Validation

The designed boost DC/DC converter is evaluated under resistor load by placing a resistor R_L at its DC output. The voltage control loop is opened and the current command is set as $i_L^* = 3$A, the measured steady-state inductor current under ($R_L = 25\Omega$, $V_{pv} = 22$V) is plotted in Fig. 5(a). The current ripple $\Delta i_L \approx 0.98$A shown in Fig. 5(a) is a little less than the analytic value $\Delta i_L = V_{pv}/(2Lf_{sd}) = 1.23$A. The measured ($i_L^*$, i_L') due to a step inductor current command change of $i_L^* = 3\text{A} \rightarrow 4\text{A}$ are shown in Fig. 5(b). The results shown in Figs. 5(a) and 5(b) indicate good static and dynamic current responses are obtained by the developed DC/DC converter.

Having good inductor current tracking response, the

voltage closed-loop control performance is further tested. Fig. 6(a) shows the measured (V_{dc}^*, V_{dc}') by the designed voltage scheme with different robust weighting factors (W_d = 0, 0.25, 0.5 and 0.75) due to a step voltage command change $V_{dc}^* = 50\text{V} \rightarrow 55\text{V}$ at ($V_{pv} = 22\text{V}$, $V_{dc}^* = 50\text{V}$, $R_L = 50\Omega$), wherein the resulted (i_L^*, i_L') with W_d =0.75 are also shown. From the results, one can find that the larger W_d is adopted the faster tracking response can be obtained. However, the payoff is the larger overshoot. Under the same condition as Fig. 6(a), Fig. 6(b) shows the measured (V_{dc}^*, V_{dc}') and (i_L^*, i_L') due to a step load resistor change of $R_L = 50\Omega \rightarrow 25\Omega$ at ($V_{pv} = 22\text{V}$, $V_{dc}^* = 50\text{V}$, $R_L = 50\Omega$). Less voltage drop can be obtained with larger W_d. Accordingly, W_d =0.25 is chosen for achieving both good command tracking and load regulation responses.

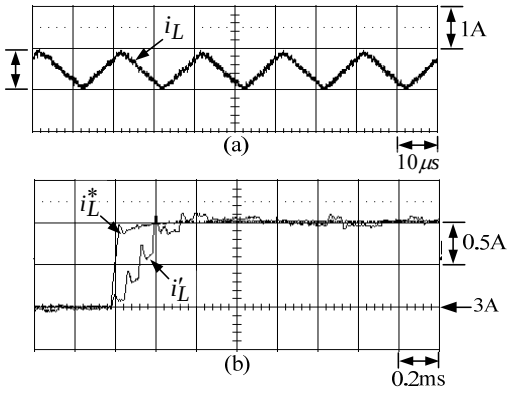

Fig. 5. Measured inductor current response under voltage open loop at ($i_L^* = 3\text{A}$, $R_L = 25\Omega$, $V_{pv} = 22\text{V}$, $V_{dc}^* = 22\text{V}$): (a) steady-state Δi_L; (b) (i_L^*, i_L') due to a step inductor current command change of $i_L = 3\text{A} \rightarrow 4\text{A}$.

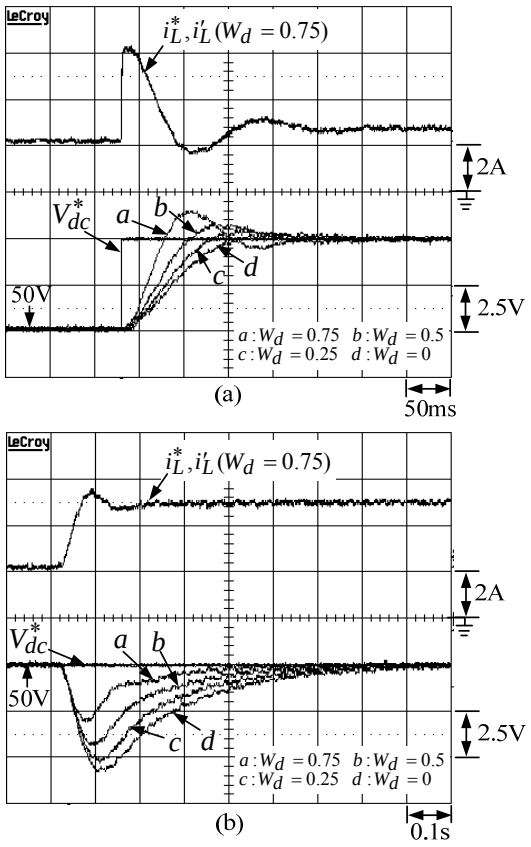

Fig. 6. Measured (V_{dc}^*, V_{dc}') and (i_L^*, i_L') with (W_d = 0, 0.25, 0.5 and 0.75) at ($V_{pv} = 22\text{V}$, $V_{dc}^* = 50\text{V}$, $R_L = 50\Omega$) due to: (a) a step voltage command change $V_{dc}^* = 50\text{V} \rightarrow 55\text{V}$; (b) a step load resistor change $R_L = 50\Omega \rightarrow 25\Omega$.

V. Performance Evaluation of Whole PMSM Driven Reaction Wheel System

(i) Normal Operation

The measured (ω_r^*, ω_r'), (i_{qs}^*, i_{qs}') and (V_{dc}^*, V_{dc}') of the established voltage-boostable PMSM driven reaction wheel system at ($V_{pv} = 22\text{V}$, $V_{dc} = 30\text{V}$) due to a step speed command change of $\omega_r^* = 1000 \rightarrow 1100\text{rpm}$ are shown in Fig. 7. Normal motor driving performance is observed, and the DC-link voltage is also well-regulated at the set level.

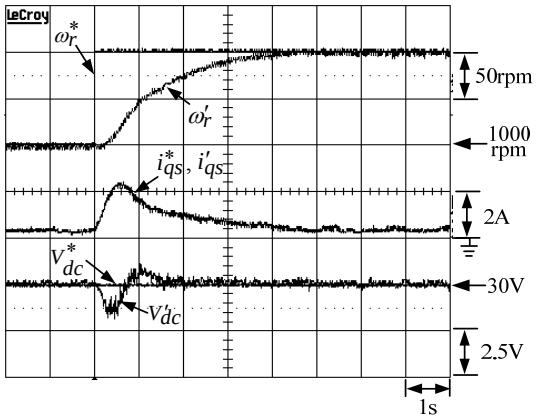

Fig. 7. Measured (ω_r^*, ω_r'), (i_{qs}^*, i_{qs}') and (V_{dc}^*, V_{dc}') at ($V_{pv} = 22\text{V}$, $V_{dc} = 30\text{V}$) due to a step speed command change of $\omega_r = 1000 \rightarrow 1100\text{rpm}$.

(ii) Effectiveness of DC-link Voltage Boosting

To evaluate the effectiveness of DC-link voltage boosting, the PMSM reaction wheel is driven at the PV cell voltage margins, i.e., $V_{dc} = 22\text{V}$ and 38V. The steady-state motor phase currents and their commands (i_{as}^*, i_{as}') with and without DC-link boosting at 1300rpm ($V_{pv} = 22\text{V}$, $V_{dc} = 22\text{V}$) and 2150rpm ($V_{pv} = 38\text{V}$, $V_{dc} = 38\text{V}$) are plotted in Figs. 8(a) and 8(b). Without voltage boosting, the phase current tracking errors exit as shown in the upper part of Figs. 8(a) and 8(b). Slightly boosting the DC-link voltage as ($V_{pv} = 22\text{V}$, $V_{dc} = 24\text{V}$) and ($V_{pv} = 38\text{V}$, $V_{dc} = 42\text{V}$) can improve this phenomenon as indicated in the lower parts of Figs. 8(a) and 8(b).

The measured (ω_r^*, ω_r'), (i_{qs}^*, i_{qs}') and (V_{dc}^*, V_{dc}') due to a step speed command change from $\omega_r = 1750 \rightarrow 2000\text{rpm}$ at ($V_{pv} = 22\text{V}$, $V_{dc} = 30\text{V}$) and ($V_{pv} = 22\text{V}$, $V_{dc} = 36\text{V}$) are compared in Figs. 9(a) and 9(b). One can observe that the lower DC-link voltage yields torque current tracking error. This will degrade the motor torque generating capability. As the operating speed is further increased (not shown here), the motor will not establish the preset speed.

(iii) The Effect of Dynamic Braking

In the dynamic braking control scheme shown in Fig 1(a), the DC-link voltage tracking error ε_{vb} is regulated by a hysteresis comparator (band $\Delta v = \pm 3\text{V}$) to yield the braking resistor chopping control signal. Let ($V_{pv} = 22\text{V}$, $V_{dc}^* = 30\text{V}$), the measured ω_r' and V_{dc} under speed pattern $\omega_r' = 0 \rightarrow 1000 \rightarrow 0\text{rpm}$ without and with dynamic braking are shown in Figs. 10(a) and 10(b). As observed from Fig. 10(a) in deceleration period, without applying dynamic braking, the DC-link voltage is increased to about 78V to initiate the inhibition of DC/DC boost converter switching operation. While in Fig. 10(b), the regenerative energy is absorbed by dynamic resistor R_b to let the DC-link voltage be well-regulated around the voltage command $V_{dc}^* = 30\text{V}$.

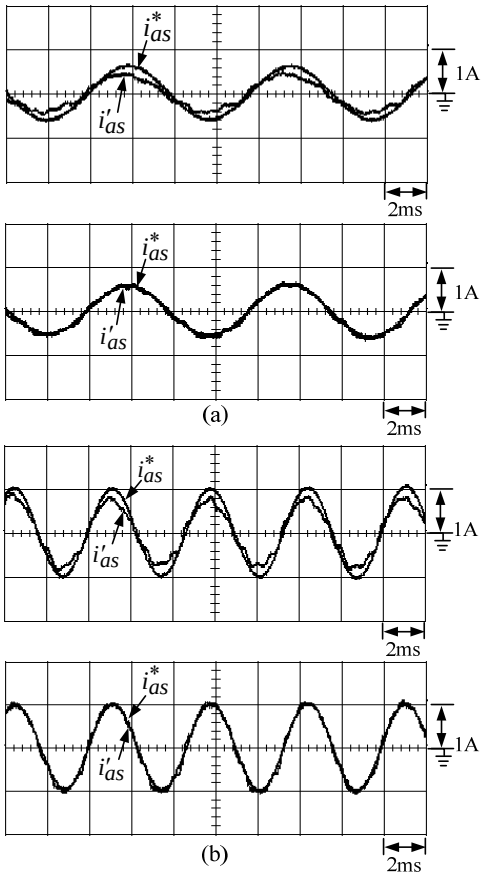

Fig. 8. Measured (i^*_{as} , i'_{as}) at PV cell voltage margins under: (a) 1300rpm without ($V_{pv}=22\text{V}$, $V_{dc}=22\text{V}$, upper) and with ($V_{pv}=22\text{V}$, $V_{dc}=24\text{V}$, lower) DC-link boosting; (b) 2150rpm without ($V_{pv}=38\text{V}$, $V_{dc}=38\text{V}$, upper) and with ($V_{pv}=38\text{V}$, $V_{dc}=42\text{V}$, lower) DC-link boosting.

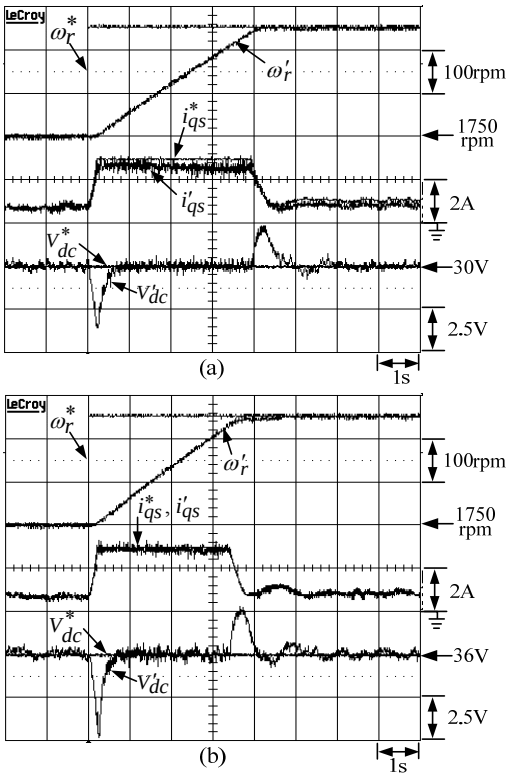

Fig. 9. Measured (ω^*_r , ω'_r), (i^*_{qs} , i'_{qs}) and (V^*_{dc} , V'_{dc}) due to a step speed command change from $\omega_r = 1750 \rightarrow 2000\text{rpm}$ at: (a) ($V_{pv}=22\text{V}$, $V_{dc}=30\text{V}$); (b) ($V_{pv}=22\text{V}$, $V_{dc}=36\text{V}$).

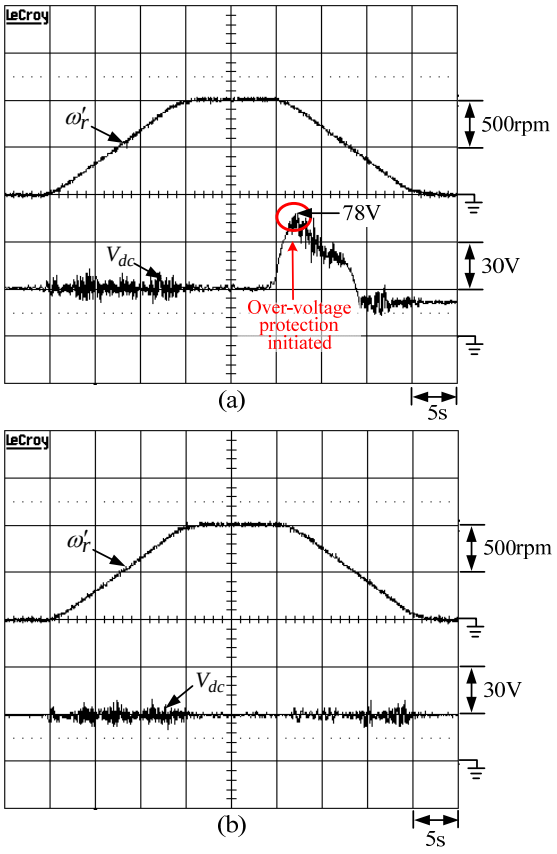

Fig. 10. Measured ω'_r and V_{dc} under speed pattern $\omega'_r = 0 \rightarrow 1000 \rightarrow 0\text{rpm}$ at ($V_{pv}=22\text{V}$, $V^*_{dc}=30\text{V}$): (a) without dynamic braking (b) with dynamic braking.

(iv) DC-link Voltage Boosting Profile

As generally recognized, the DC-link voltage should be properly set [14,15,18,19] in accordance with the motor running speed to achieve better driving performance and efficiency. In the developed PMSM driven reaction wheel system shown in Fig. 1(a), a simple DC-link voltage profile is suggested in Fig. 11, where ω_b and ω_m are the base and maximum motor speed respectively. The minimal DC-link voltage is set as $V_{dc}=38\text{V}$ owing to the boosting nature of the adopted DC/DC converter. Obviously, the DC-link voltage can also be set according to the sensed actual PV voltage. In addition to the static voltage boosting, a dynamic boosting voltage can also be added according to the wingding current tracking errors as shown in Fig. 1(a). Further research results will be presented in the near future.

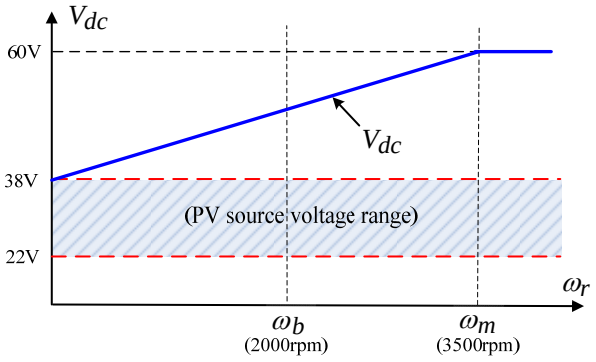

Fig. 11. DC-link voltage boosting profile.

VI. CONCLUSIONS

The establishment of a PMSM driven satellite reaction wheel with voltage boostable DC-link and its dynamic controls have been presented in this paper. The proposed current control scheme consists of a PI feedback controller, an adaptive resonant feedback controller and a simple robust tracking error cancellation controller. Excellent sinusoidal current command tracking characteristics under reasonable DC-link voltage level are achieved. In speed control, the quantitatively designed PI feedback controller is augmented with simple robust control to preserve the defined reference speed response trajectory.

To let the reaction wheel be operated within broad speed range under fluctuated PV source voltage, this paper developed a boost DC/DC converter front-end to establish boostable and well-regulated DC-link voltage for the PMSM drive from the PV cell. The whole PMSM driven satellite reaction wheel equipped with DC/DC boost converter is evaluated experimentally. The results indicated that DC-link voltage boosting can yield improved driving performance under varying speed. However, the more suited voltage boosting strategy and the more detailed performance assessment are needed to be further studied.

VII. REFERENCES

[1] E. Lee, "A micro HTS renewable energy/attitude control system for micro/nano satellites," *IEEE Trans. Appl. Supercond.*, vol. 13, no. 2, pp. 2263-2266, Jun. 2003.

[2] S. J. Dodds and J. Vittek, "Spacecraft attitude control using an induction motor actuated reaction wheel with sensorless forced dynamic drive," in *IEE Colloq. All Elect. Aircraft Dig.* 1998/260, Jun. 1998, pp. 9/1-9/7.

[3] B. H. Kenny, R. Jansen, P. Kascak, T. Dever and W. Santiago, "Integrated power and attitude control with two flywheels," *IEEE Trans. Aerosp. Electron. Syst.*, vol. 41, no. 4, pp. 1431-1449, Oct. 2005.

[4] A. Altay and O. Tekinalp, "Spacecraft energy storage and attitude control," in *Proc.RAST*, 2005, pp. 201-206.

[5] P. C. Krause, O. Wasynczuk and S. D. Sudhoff, *Analysis of Electric Machinery and Drive Systems*, 2nd ed. New York: Wiley-IEEE, 2002.

[6] E. D. Ganev, "High-Performance electric drives for aerospace more electric architectures part I- electric machines," in *Proc. IEEE Power Engineering Society General Meeting*, June 2007, pp. 1-8.

[7] S. Fukuda and R. Imamura, "Application of a sinusoidal internal model to current control of three-phase utility-interface converters," *IEEE Trans. Ind. Electron.*, vol. 52, no. 2, pp. 420-426, April 2005.

[8] W. Lenwari, M. Summer, P. Zanchetta and M.Culea, "A high performance harmonic current control for shunt active filters based on resonant compensators," in *Proc. IECON*, Nov. 2006, pp. 2109-2114.

[9] D. N. Zmood, D. G. Holmes and G. Bode, "Frequency domain analysis of three phase linear current regulators," *IEEE Trans. Ind. Appl.*, vol. 37, no. 2, pp. 601-610, Mar/Apr 2001.

[10] M. C. Chou and C. M. Liaw, "Development of robust current 2-DOF controllers for a permanent magnet synchronous motor drive with reaction wheel load," *IEEE Trans. Power Electron.*, vol. 24, no. 5, pp. 1304-1320, May 2009.

[11] K. Yamamoto, K. Shinohara and H. Makishima, "Comparison between flux weakening and PWM inverter with voltage booster for permanent magnet synchronous motor drive," in *Proc. PCC*, 2002, vol. 1, pp. 161-166.

[12] A. Fratta, P. Guglielmi, F. Villata and A. Vagati, "Efficiency and cost-effectiveness of AC drives for electric vehicles improved by a novel boost DC-DC Conversion structure," in *Proc. PET*, 1998, pp. 11-19.

[13] H. Matsumoto, "Experiment of boost motor driver with EDLCs," *Electron. Letters*, vol. 45, no. 12, pp. 654-655, June 2009.

[14] K. Yamamoto, K. Shinohara and T. Nagahama, "Characteristics of permanent-magnet synchronous motor driven by PWM inverter with voltage booster," *IEEE Trans. Ind. Appl.*, vol. 40, no. 4, pp. 1145-1152, 2004.

[15] K. Asano, Y. Inaguma, H. Ohtani, E. Sato, M. Okamura and S. Sasaki, "High performance motor drive technologies for hybrid vehicles," in *Proc. PCC'07*, 2007, pp. 1584-1589.

[16] F. Caricchi, F. Crescimbini and A. Di Napoli, "20kW water-cooled prototype of a buck-boost bidirectional DC-DC converter topology for electrical vehicle motor drives," in *Proc. APEC'95*, 1995, vol. 2, pp. 887-892.

[17] F. Caricchi, F. Crescimbini, F. Giulii Capponi and L. Solero, "Study of bi-directional buck-boost converter topologies for application in electrical vehicle motor drives," in *Proc. APEC'98*, 1998, vol. 1, pp. 287-293.

[18] J. H. Kim, H. S. Kang, B. K. Lee and J. Hur, "Cost Effective PAM inverter for 42V hybrid electric vehicles (HEV)," in *Proc. VPPC'08*, 2008, pp. 1-6.

[19] A. M. Howlader, N. Urasaki, Y. Senjyu and A. Yona, "Wide-speed-range optimal PAM control for permanent magnet synchronous motor," in *Proc. ICEMs*, 2009, pp. 1-5.